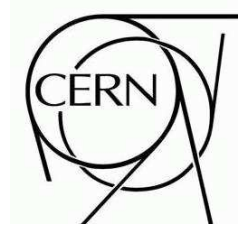# ATLAS NOTE

A Simple p_T- and η-Dependent Monte Carlo-Based Jet Calibration

D. López Mateos[1,2], E. W. Hughes[1], and A. Schwartzman[3]

[1] *Columbia University, New York, NY 10027, USA*
[2] *California Institute of Technology, Pasadena, CA 91125, USA*
[3] *SLAC National Accelerator Laboratory, Menlo Park, CA 94025, USA*

Abstract

The determination of the jet energy scale will be of key importance to many LHC physics analyses. Several techniques exist that attempt to determine the jet energy scale, improve the jet energy resolution, or perform both at the same time. In this note we present a Monte Carlo-based method to calibrate electromagnetic-scale jets by inverting the response function. The techniques presented in this note are useful for all calibration procedures that require inverting a response function, such as the data-driven calibration using (γ, Z)+jet balance, and even the cell-energy-density and local-hadron calibrations. The calibration has been derived for ATLAS cone jets of radius 0.4 made of towers and topo-clusters, but can be easily extended to jets reconstructed with other algorithms or constituents.

Contents

1 Introduction

An accurate jet calibration will be needed for a variety of measurements that can be performed at the LHC: ranging from QCD analyses to top quark studies and new physics searches. In ATLAS, the cell-energy-density [1] (H1-style) and local-hadron [2] calibrations have been studied in detail and used for physics studies with Monte Carlo simulations. These calibration schemes use the Monte Carlo simulation to derive the calibration constants. More recently, also calibration techniques that are derived directly from ATLAS data have started to be studied. In this effort, calibration and resolution improvement are well-separated tasks, and involve different techniques. A possible calibration sequence is shown in Figure 1.
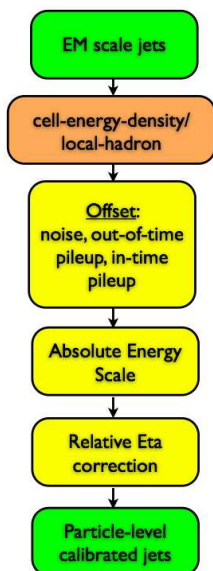

Figure 1: Flow of corrections taking jets from their uncalibrated state (electromagnetic-scale jets) to their calibrated state. Improvements in the jet energy resolution can be obtained with data-driven techniques after the calibration (not shown), or Monte Carlo-based techniques, before or after the calibration (H1-style and local-hadron calibrations shown).

In this note, the corrections before the offset correction are ignored for simplicity. The offset correction, is currently under study; but it will only be relevant for events with pile-up (i.e.: several minimum bias interactions accompanying the hard scattering). For this reason it is also ignored in this document. In events without pile-up, like those used so far for most Monte Carlo studies, the calibration is reduced to a simple p_T- and η-dependent correction. This simple calibration can be derived using (γ, Z)+jet or di-jet balancing techniques. It consists of measuring and inverting the jet energy response function, to restore the correct energy scale. Further data-driven corrections that aim at improving the resolution can be applied after the simple calibration sequence outlined above is implemented.

A simple Monte Carlo-based calibration that performs the inversion of the jet response function is necessary for the following reasons:

1. It provides a performance baseline for jets with the correct energy scale. This is useful to evaluate the resolution improvements provided by more sophisticated techniques and is further discussed in Appendix A.

2. It provides a simple calibration for the very first data, even before there is enough data to obtain a reliable data-driven calibration.

3. It allows for the study of certain resolution improvement techniques using Monte Carlo. These techniques need jets calibrated with a simple data-driven calibration as their input. In the absence of data, the study of these techniques can only be performed with a Monte Carlo-based calibration that also inverts the response.

4. It allows physics groups to compare the performance of their analyses with a simple calibration and with more complex techniques such as the H1-style calibration. This can be very useful for early-data analyses, where a simple calibration might be better understood than the more sophisticated calibration methods.

In this note we derive a simple Monte Carlo-based calibration for jets reconstructed with the ATLAS cone algorithm [3] with radius 0.4 (cone 0.4 jets) using two different input constituents: towers and topological clusters (topo-clusters) [1]. The calibration is derived for these constituents because they are currently the two default jet constituents in ATLAS. The main difference between them is that towers are detector objects with a fixed geometry, while topo-clusters are dynamic objects built using adjacent cells with a significant signal. The complex geometry of a topo-cluster is meant to capture better the shower of a single particle. Topo-clusters are also noise-suppressed by construction. Note, however, that the techniques described in this note are applicable to jets built up of other constituents too.

The event selection is described in detail in Section 2. We explain the details of the *numerical inversion* technique used in the derivation of the calibration in Section 3. Finally, Section 4 shows some of the results obtained with this calibration, including comparisons with jets calibrated using the H1-style calibration method.

2   Monte Carlo Samples, Event Selection and Event Reconstruction

For the studies in this document, two data samples are used: a high statistics di-jet sample made of four ATLAS data sets, and a Z+jets sample with the Z's decaying to di-muons. The former is used to derive and validate the calibration. To avoid performing the validation exclusively on events fully correlated to those used in its derivation, the second sample is used as part of the validation too. The names of the data sets used are listed in Table 1.

	Production Datasets		
Z+jets	mc08.106051.PythiaZmumu_1Lepton.recon.AOD.e347_s462_r541		
Dijets	mc08.105011.J2_pythia_jetjet.recon.AOD.e344_s475_r586 mc08.105012.J3_pythia_jetjet.recon.AOD.e344_s475_r586 mc08.105013.J4_pythia_jetjet.recon.AOD.e344_s475_r586 mc08.105014.J5_pythia_jetjet.recon.AOD.e344_s475_r586		

Table 1: Production datasets used in this document.

For the derivation of the correction as well as for its validation, reconstructed cone 0.4 jets with a matched truth particle jet within a radius of 0.3 in $\eta \times \phi$ space are used. This matching radius rejects very few jets even at low p_T, as shown in Figure 2. The performance of the correction is stable against the maximum matching radius chosen for matching radii ranging from 0.2 to 0.7 to be discussed in Section 4.
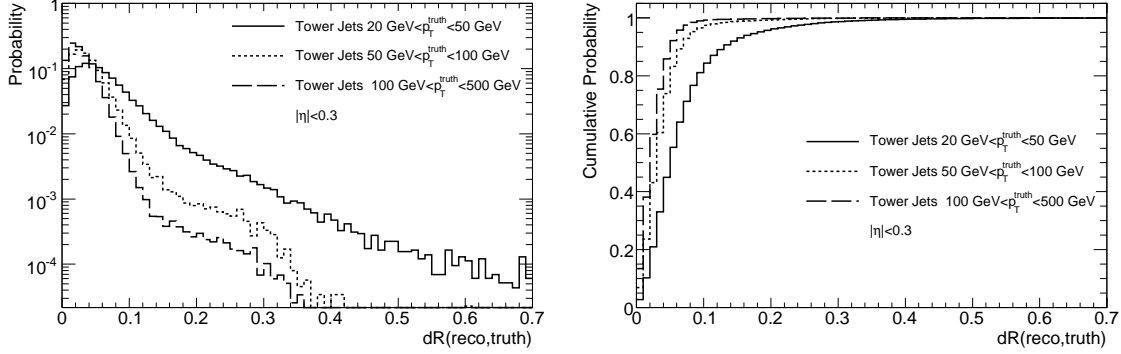
Figure 2: Left: Probability distribution for cone 0.4 tower jets with $|\eta_{\mathrm{EM}}^{\mathrm{reco}}| < 0.3$ from the di-jet sample as a function of truth matching radius. Distributions are shown for jets with $20\,\mathrm{GeV} < p_T^{\mathrm{true}} < 50\,\mathrm{GeV}$ (solid line), $50\,\mathrm{GeV} < p_T^{\mathrm{true}} < 100\,\mathrm{GeV}$ (dotted line) and $100\,\mathrm{GeV} < p_T^{\mathrm{true}} < 500\,\mathrm{GeV}$ (dashed line). The matching radius is the distance in $\eta \times \phi$ space between the reconstructed jet and the closest truth particle jet. The jets used were *isolated* as defined in the text. Right: Cumulative probability of the same quantities shown on the left plot.

Jets used in the derivation of the correction and the validation are also required to be *isolated*. In the di-jet sample, the isolation requirement tries to remove jets that are split, and are thus close to each other. This is achieved requiring that the reconstructed jet does not have another reconstructed jet within a radius of 1.0. Split jets are expected to have a different energy scale and should be treated separately. The development of such treatment is beyond the scope of this note.

In the Z+jets sample, an additional isolation requirement is added to remove from the sample high-energy muons that lose a substantial fraction of their energy in the calorimeter. This is achieved requiring that the jets used do not have the two leading reconstructed muons (reconstructed by either Muonboy or STACO [1]) within a radius of 0.5. Jets are also required to have $\Delta\phi > 2.7$ with respect to the true ϕ of the Z-boson. This favors the selection of quark jets over gluon jets from final-state radiation. Since the di-jet sample is dominated by gluon jets, this selection allows investigating the effect of flavor in the jet response.

The correction is derived in rather coarse bins of $\eta_{\mathrm{EM}}^{\mathrm{reco}}$, the reconstructed η of jets at the electromagnetic scale, to mimic what the first data-driven calibrations may look like. However, in η regions where the response variations are most dramatic, the binning is finer. The bins used are those limited by the following $|\eta|$ values: 0.3, 0.8, 1.4, 1.5, 1.6, 1.7, 2.1, 2.8, 2.9, 3.0, 3.1, 3.2, 3.3, 3.4, 3.5, 3.6, 4.5. In the rest of this note η refers to the reconstructed η of the jet for the calibration being considered (i.e.: $\eta_{\mathrm{H1}}^{\mathrm{reco}}$ for jets calibrated in the H1 style, $\eta_{\mathrm{EM}}^{\mathrm{reco}}$ for electromagnetic-scale jets, ...).

The Z+jets sample was simulated with detector conditions (OFL-COND-00-00-03) that represent the calorimeter status as it was at the end of 2008. Some regions were, thus, not operational. In order to obtain a uniform response in ϕ and to make meaningful comparisons with the di-jet dataset (reconstructed with ideal detector conditions), a set of fiducial cuts was applied in the different η bins. This set of cuts is summarized in Table 2 and is further discussed in Appendix B.

3   Numerical Inversion Technique

The simple calibration derived in this note is based on the inversion of the response function $R(p_T^{\mathrm{reco}}) = p_T^{\mathrm{reco}}/p_T^{\mathrm{true}}$, where p_T^{reco} refers in our case to the reconstructed p_T at the electromagnetic scale, $p_{T,\mathrm{EM}}^{\mathrm{reco}}$. Given the response function $R(p_T^{\mathrm{reco}})$, the p_T of a jet can be estimated as $p_T^{\mathrm{reco}}/R(p_T^{\mathrm{reco}})$. However, it is

η region	ϕ region(s) excluded
$[-3.3, -1.4]$	$[-2, 0.4]$
$[0, 0.3]$	$[-1.6, -0.6]$
$[0.3, 0.8]$	$[-1.6, -0.6]$, $[2, 3]$
$[1.7, 2.8]$	$[-0.2, 1.2]$

Table 2: Fiducial cuts used for jets from the Z sample.

not clear how to parameterize the response as a function of p_T^{reco}, because for fixed p_T^{reco} the response distribution is not Gaussian. On the other hand, the calorimeter response for jets of fixed p_T^{true} is Gaussian, as illustrated in Figure 3. The shape of the distribution for bins of p_T^{reco} is determined by the underlying
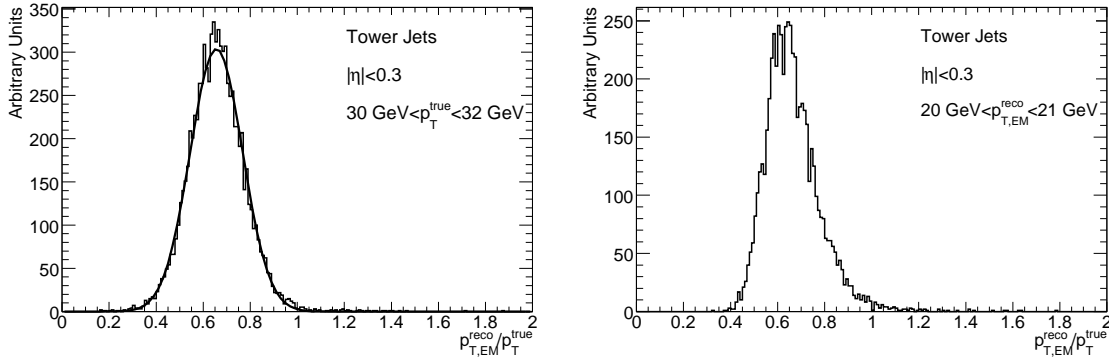

Figure 3: Left: Response distribution for tower jets of $30\,\text{GeV} < p_T^{\text{true}} < 32\,\text{GeV}$ from the di-jet sample. The Gaussian fit is overlaid. Right: Response distribution for tower jets of $20\,\text{GeV} < p_{T,\text{EM}}^{\text{reco}} < 21\,\text{GeV}$ from the di-jet sample. The limits of the $p_{T,\text{EM}}^{\text{reco}}$ bin are chosen so that the same kinematic region of the calorimeter is explored (i.e.: jets with $p_T^{\text{true}} \approx 30$ GeV will be on average reconstructed with $p_{T,\text{EM}}^{\text{reco}} \approx 20$ GeV using the mean response from the plot on the left).

falling p_T spectrum of the jet distribution. Since the cross-section is higher low-p_T^{true} jets, for any fixed p_T^{reco} bin, there will be more jets with low p_T^{true} (i.e.: high response). This causes a tail towards the high-response end of the response distribution.

The *numerical inversion* technique has already been used in ATLAS previously [4] to solve a problem similar to this. In essence, this technique allows applying p_T-dependent calibrations to reconstructed jets when the average response of these jets has a dependence on p_T^{true}. As such, it can be used with electromagnetic-scale jets (as in this note), but also with jets calibrated by other means (e.g.: local-hadron calibration) as a final step to remove any residual dependence of the response as a function of p_T. There are two steps to this technique:

1. Calculation of $R(p_T^{\text{true}})$ from the Gaussian R distributions in different p_T^{true} bins.

2. Estimation of $R(p_T^{\text{reco}})$ using the following equation, that holds on average: $p_{T,\text{est}}^{\text{reco}} = R(p_T^{\text{true}}) \cdot p_T^{\text{true}}$.

Note that $R(p_T^{\text{reco}})$ is, in fact, calculated as a function of $p_{T,\text{est}}^{\text{reco}}$. However, when it is used as part of the calibration it is evaluated on a jet-by-jet basis as a function of the jet p_T^{reco}. For this reason, in the rest of the note, p_T^{reco} and $p_{T,\text{est}}^{\text{reco}}$ may be used interchangeably in this context, depending on whether the emphasis is on how the R function is calculated or how it is used.

With an expression for $R(p_T^{\text{reco}})$, the jet can be calibrated through the inversion of the response as $p_T^{\text{calib}} = p_T^{\text{reco}}/R(p_T^{\text{reco}})$. The jet four-momentum is calibrated in an equivalent way: using $R(p_T^{\text{reco}})$ as a

scale factor for each of its components. The technique can also be used in data-driven techniques that calculate the response as a function of some unbiased estimate of the jet p_T such as p_T^γ in γ+jets events. In this case, the unbiased estimate would substitute p_T^{true} in the steps outlined above.

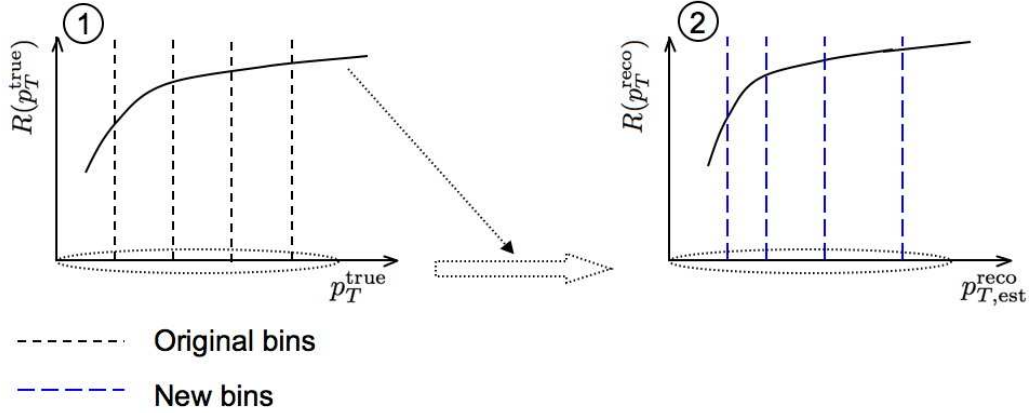The two steps of the numerical inversion are illustrated in Figure 4. As indicated by this illustration,

Figure 4: Illustration of the process carried out by the numerical inversion technique as explained in the text.

the response calculated in step 1 is used to transform the x-axis of the response graph. This transformation can be done for each point in the graph, or for all jets entering the calculation of each point of the graph. The first option is more convenient when it is difficult to find a parameterization of $R(p_T^{\text{true}})$, as it might be the case when parameterizing as a function of p_T^{true} and another variable.

For this note we use the second option. That is, we first fill a 2-D histogram, with axes R and p_T^{true}. Gaussian fits to R for different p_T^{true} bins are used to build $R(p_T^{\text{true}})$ and the points defining this function are fit to

$$\sum_{i=0}^{4} \frac{a_i}{(\ln(p_T[\text{ GeV}]))^i}, \tag{1}$$

with $a_0 = 1$ and a_i are free parameters. In step 2, we refill the 2-D histogram, this time using $R(p_T^{\text{true}}) \cdot p_T^{\text{true}}$ for the p_T axis. The response function is built again using this new histogram, and fit to Equation 1. This fit is what we call $R(p_{T,\text{EM}}^{\text{reco}})$, and it is our calibration function. The procedure is illustrated in Figure 5.

The numerical inversion procedure handles the non-Gaussian nature of the response distribution for fixed p_T^{reco}. As explained above this is a consequence of the underlying jet p_T spectrum. This technique is not relevant when calibrating calorimeters in contexts where this is not an issue (e.g.: when using single-particle monochromatic beams).

4 Validation

In this section we validate the calibration obtained with the method described in the previous section. Here we show the most representative plots. The calibration constants and additional validation plots are given in Appendix C.

4.1 p_T Response Studies

The main goal of any calibration is to achieve a p_T-independent response centered at 1. Figure 6 shows the response as a function of p_T^{true} for jets from the di-jet sample for different η bins for the H1-style
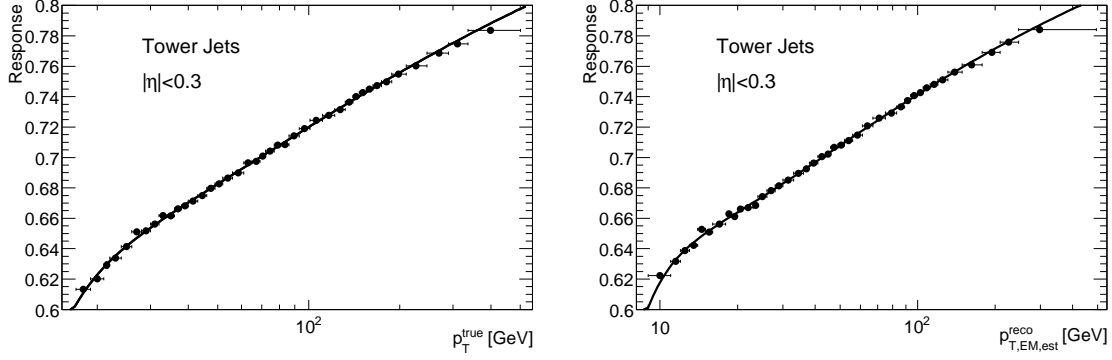
Figure 5: Illustration of the process carried out by the numerical inversion technique with data from the di-jet sample. In the first step (left) a fit to $R(p_T^{\text{true}})$ is performed. In the second step, the fit from the first step is used to transform the x-axis of the plot on the left, giving the plot on the right. This is then fit to the same function, giving $R(p_{T,\text{EM}}^{\text{reco}})$. Each point in these graphs contains equal number of jets and the p_T position of the points is determined by the mean p_T of the jets in the corresponding response distribution.

calibration and the simple calibration based on the numerical inversion. The numerical-inversion jets
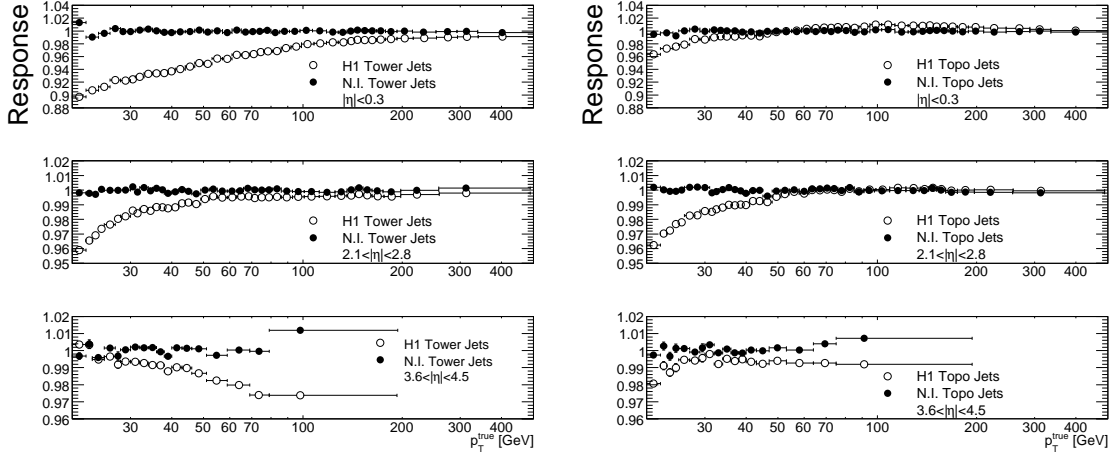

Figure 6: Response as a function of p_T^{true} for cone 0.4 tower (left) and topo-cluster jets (right) with the H1-style calibration (hollow points) and the numerical-inversion calibration (solid points). Three η regions are used: a central region (top, $|\eta| < 0.3$), an intermediate region (middle, $2.1 < |\eta| < 2.8$) and a forward region (bottom, $3.6 < |\eta| < 4.5$).

have a more uniform response than the H1-style calibration jets in the current release.

The response shapes are different for topo-cluster and tower jets because the same weights are used to correct both types of jets, while the cell energy densities change after the noise subtraction performed by the topo-clustering algorithm. The non-linearity for both types of jets arises due to several effects. One of the effects is a mathematical bias that has been reported in [5]. Another relevant effect occurs because the H1-style calibration has been derived with a maximum matching radius for reconstructed to true jets ($dR_{\text{max}}^{\text{truth}}$) of 0.2. As explained in Section 2, we are showing the response for all isolated jets with $dR_{\text{max}}^{\text{truth}}$=0.3. Jets that are reconstructed far away from their corresponding true jet will have lower response, because not all particles in the jet fall within the reconstructed cone. Therefore, the jets used in deriving the H1-style calibration have a bias towards higher response values. This leads to an overall

lower response when jets with larger matching radii are considered.

This effect can be observed if we apply the numerical inversion correction extracted with $dR = 0.3$ to jets varying $dR_{\text{max}}^{\text{truth}}$. This is shown for jets with $|\eta| < 0.3$ in Figure 7. The left plot shows the response
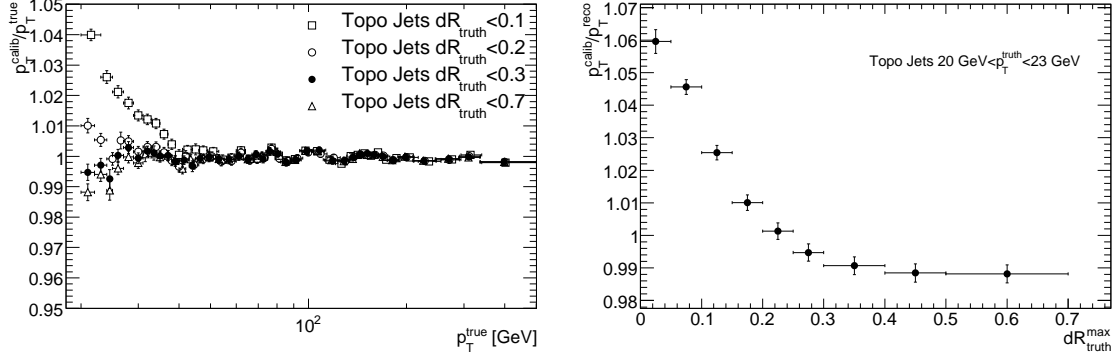

Figure 7: Left: Response as a function of p_T^{true} for cone 0.4 topo-cluster jets of $|\eta| < 0.3$ for different upper bounds on the matching radius between reconstructed and true jet. Right: Response for a low-p_T bin as a function of the upper bound on the matching radius ($dR_{\text{truth}}^{\text{max}}$).

as a function of p_T^{true} for different values of $dR_{\text{max}}^{\text{truth}}$. Clearly the effect is most significant at low p_T. The response also increases more rapidly for $dR_{\text{max}}^{\text{truth}} < 0.2$. This is also shown on the right plot, where the response is shown as a function of $dR_{\text{max}}^{\text{truth}}$ for a low-p_T bin. The response becomes stable for $dR_{\text{max}}^{\text{truth}} \gtrsim 0.3$. This, together with the results shown in Figure 2, justifies the choice of $dR_{\text{max}}^{\text{truth}} = 0.3$. The p_T dependence of these plots is due to the angular resolution of the calorimeter, and it is further discussed in Section 4.3.

The response as a function of η has also been studied, and can be best summarized by the plots shown in Figure 8. The response for the H1-style calibration is centered at ≈ 1 for topo-cluster jets,
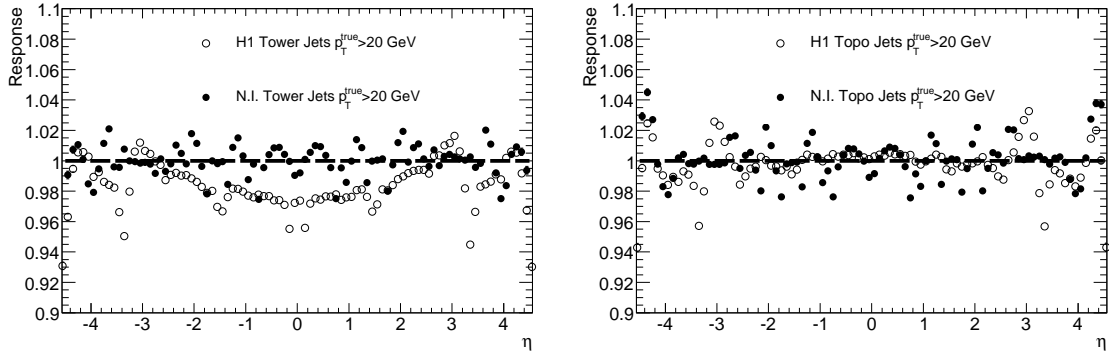

Figure 8: Response as a function of η for cone 0.4 tower (left) and topo-cluster jets (right) of $p_T^{\text{true}} > 20$ GeV. Jets calibrated with the numerical-inversion calibration (solid points) and the H1-style calibration (hollow points) are shown.

and it is a bit low in the barrel for tower jets. The response for the numerical inversion calibration is also centered at ≈ 1 with fluctuations of $\approx 3\%$. These fluctuations are partially due to the rather coarse binning in η used in the calibration, and are absent in the regions where a finer binning was chosen (e.g.: $2.8 < |\eta| < 3.6$). The pattern in the response after numerical inversion can only be understood when the binning effects are considered together with the varying response pattern at the electromagnetic scale. For reference, the response as a function of η for jets at the electromagnetic scale is shown for three
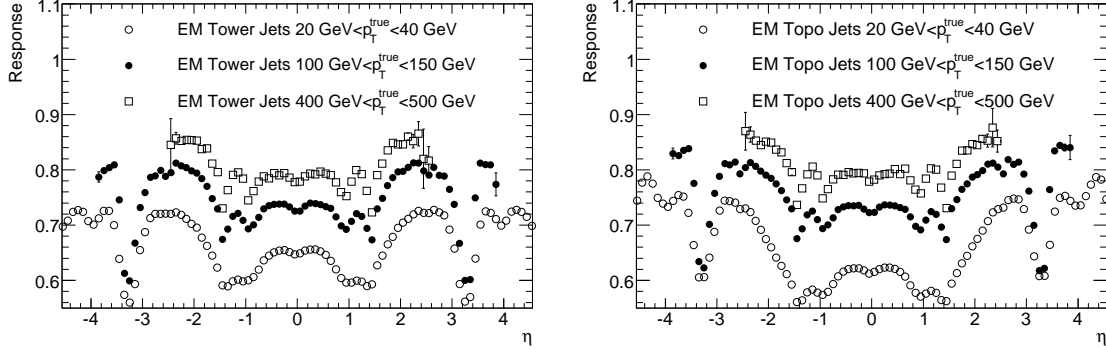
different p_T bins in Figure 9.

Figure 9: Response at the electromagnetic scale as a function of η for cone 0.4 tower (left) and topo-cluster jets (right) of 20 GeV $< p_T^{\text{true}} <$ 40 GeV (hollow circles), 100 GeV $< p_T^{\text{true}} <$ 150 GeV (solid circles) and 400 GeV $< p_T^{\text{true}} <$ 500 GeV (hollow squares).

The response has also been studied in the Z +jets sample. This sample is statistically independent from the di-jet sample, so it allows studying the statistical uncertainty associated with the numerical inversion calibration. In addition, the p_T spectrum of jets in this sample is different from that of the di-jet sample, so any bias correlated with the form of this spectrum can also be studied.

With the event selection used in this sample, jets are expected to be mostly quark jets, particularly in the barrel region. Quark jets have, in principle, a higher average response than gluon jets because they have a harder fragmentation. Since the di-jet sample is composed of a mixture of gluon and quark jets, the response is expected to be higher in the Z +jets sample than in the di-jet sample. Thus, this study can be used to estimate the magnitude of these flavor effects, combined with the statistical and p_T-spectrum effects mentioned above.

The response as a function of p_T^{true} for jets from the Z +jets sample in the same η regions as in Figure 6 is shown in Figure 10. The response is systematically higher than in the di-jet sample for jets
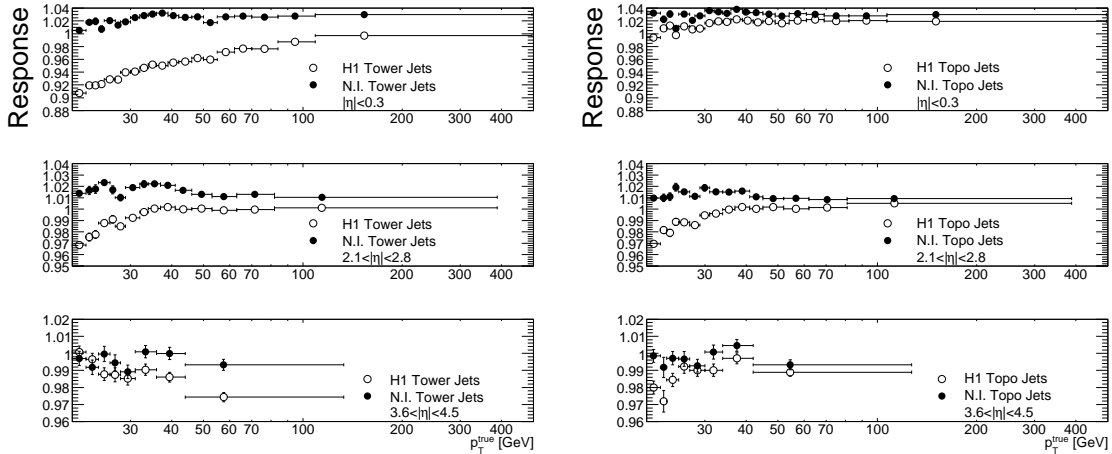

Figure 10: Response as a function of p_T for cone 0.4 tower (left) and topo-cluster jets (right) from the Z +jets sample. Jets calibrated with the H1-style calibration (hollow points) and the numerical-inversion calibration (solid points) are shown. Three η regions are used: a central region (top, $|\eta| < 0.3$), an intermediate region (middle, $2.1 < |\eta| < 2.8$) and a forward region (bottom, $3.6 < |\eta| < 4.5$).

calibrated with either technique. This effect is more pronounced for central jets. This is as expected, since our selection chooses more quark jets in the central region. In the forward region, there are more jets from final-state radiation, so there are more gluon jets. The flavor composition is then closer to that of the di-jet sample and so is the response. This effect can also be observed in Figure 11. This figure shows
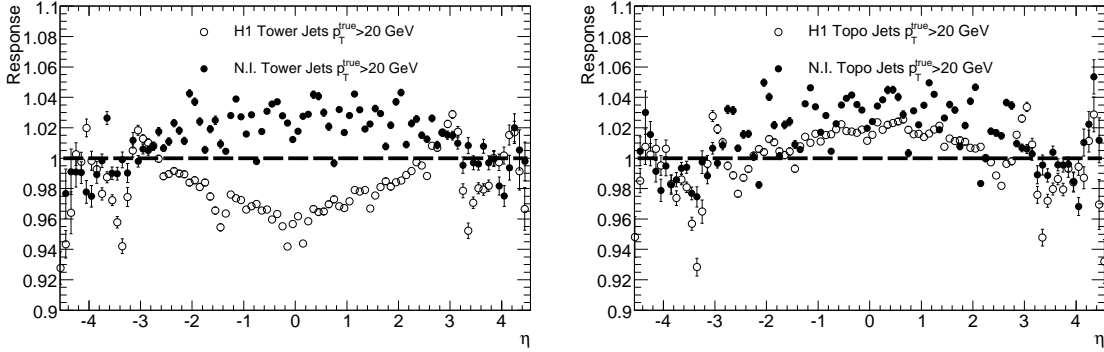

Figure 11: Response as a function of η for cone 0.4 tower (left) and topo-cluster jets (right) of $p_T^{\text{true}} >$ 20 GeV from the Z +jets sample. Jets calibrated with the numerical-inversion calibration (solid points) and the H1-style calibration (hollow points) are shown.

that the response for central jets is shifted upwards by $\approx 3\%$, while the response of forward jets remains at ≈ 1. These values set a lower bound on the systematic uncertainties if flavor-dependent corrections are ignored. The numerical-inversion calibration is accurate to $\approx 4\%$ in p_T^{true} and η, after effects of flavor, statistics and underlying p_T spectrum are considered. Samples with strong biases towards other jet flavors (e.g: b-jets) may have larger systematic biases in the response.

For jets calibrated in the H1-style, the response is only shifted upwards for topo-cluster jets, while it is shifted downwards for tower jets. This effect is due to the underlying jet spectrum and the p_T-dependence of the response. The mean p_T of jets from the Z+jets sample is lower than that of jets from the di-jet sample. This implies that jets from the Z+jets sample are probing the low-p_T part of the response, which is lower. This effect tends to pull the response for jets above 20 GeV down. The effect is pronounced for tower jets because their response after the H1-style calibration has a strong dependence with p_T. The effect is small for topo-cluster jets, so the response is higher in the Z+jets sample, showing the flavor effect discussed above.

4.2 p_T **Resolution Studies**

Another key performance measure is the jet energy resolution (the standard deviation of the response distribution). The comparison between the H1-style calibration and the numerical-inversion calibration is interesting because the latter only corrects the jet energy scale of jets, while the former is meant to also improve the resolution.

The quantity used for this comparison is not the absolute resolution, but the fractional jet energy resolution σ_R/R. For this study, only jets from the di-jet sample are used. The comparison between the different calibrations is shown in Figure 12.

Overall, topo-cluster jets perform slightly better than tower jets, particularly in the forward regions. The numerical-inversion calibration performs comparably to the H1-style calibration for jets of $p_T^{\text{true}} \lesssim 40$ GeV. For high-p_T jets the H1-style calibration performs better, as expected, especially in the barrel region ($\approx 30\%$ relative improvement at 500 GeV), but also in the forward region ($\approx 15\%$ relative improvement at 500 GeV for topo-cluster jets). For tower jets in the forward region, H1-style seems to
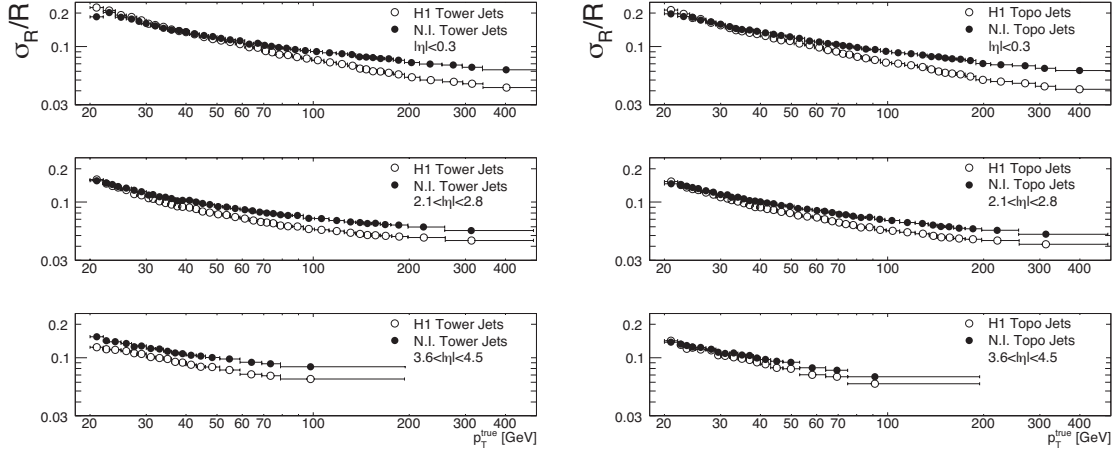
Figure 12: Fractional jet energy resolution as a function of p_T for cone 0.4 tower (left) and topo-cluster jets (right) with the H1-style calibration (hollow points) and the numerical-inversion calibration (solid points). Three η regions are used: a central region (top, $|\eta| < 0.3$), an intermediate region (middle, $2.1 < |\eta| < 2.8$) and a forward region (bottom, $3.6 < |\eta| < 4.5$).

provide a performance improvement for the full p_T range. However, this improvement is only apparent. Such apparent improvement can appear if the response is monotonically decreasing as a function of p_T (see Figure 6). A similar argument suggests that the resolution for low-p_T jets calibrated with the H1-style calibration in the central regions may appear to be worse in these plots than it would be if the jet response was flat. This topic is elaborated in Appendix A.

4.3 Angular Resolution Studies

We have also studied the angular resolution and its impact in the jet calibration. Here, as in Section 4.2, the comparison between the numerical-inversion and H1-style calibration is interesting. The H1-style calibration changes the (η, ϕ) coordinates of the jet, while the numerical-inversion calibration provides a simple scale factor to the jet four-vector, thus leaving its direction unchanged.

For these studies, we compare the width of the $\phi_{\text{reco}} - \phi_{\text{true}}$ and $\eta_{\text{reco}} - \eta_{\text{true}}$ distributions for jets from the dijet sample. We show the width of Gaussian fits to these distributions as a function of p_T^{true} in Figures 13 and 14. The mean of the distributions has also been studied, and it is 0, as desired, in the full momentum range for the η regions shown.

The features of the ϕ and η resolutions are common. In particular, when using the numerical-inversion calibration, topo-cluster jets perform better than tower jets. However, if the H1-style calibration is used, the performance is similar for both types of jets. This implies that the H1-style calibration improves the angular resolution of tower jets, but leaves the angular resolution of topo-cluster jets unchanged. This is currently not understood.

It is worth pointing out that the ϕ and η resolutions in the barrel at low p_T are ≈ 0.07 and 0.06, respectively. This leads to a radial resolution in $\eta \times \phi$ space of ≈ 0.1. This means that a $dR_{\text{max}}^{\text{truth}}$ of 0.1 cuts out $\approx 32\%$ of the jets. This confirms that the results shown in Figure 7 can be attributed to this resolution effect.
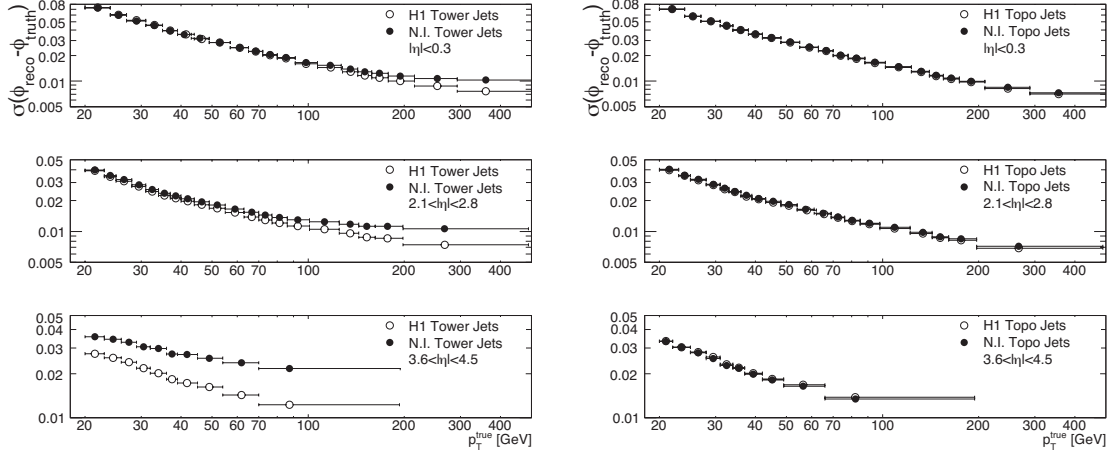
Figure 13: ϕ resolution as a function of p_T for cone 0.4 tower (left) and topo-cluster jets (right) with the H1-style calibration (hollow points) and the numerical-inversion calibration (solid points). Three η regions are used: a central region (top, $|\eta| < 0.3$), an intermediate region (middle, $2.1 < |\eta| < 2.8$) and a forward region (bottom, $3.6 < |\eta| < 4.5$).
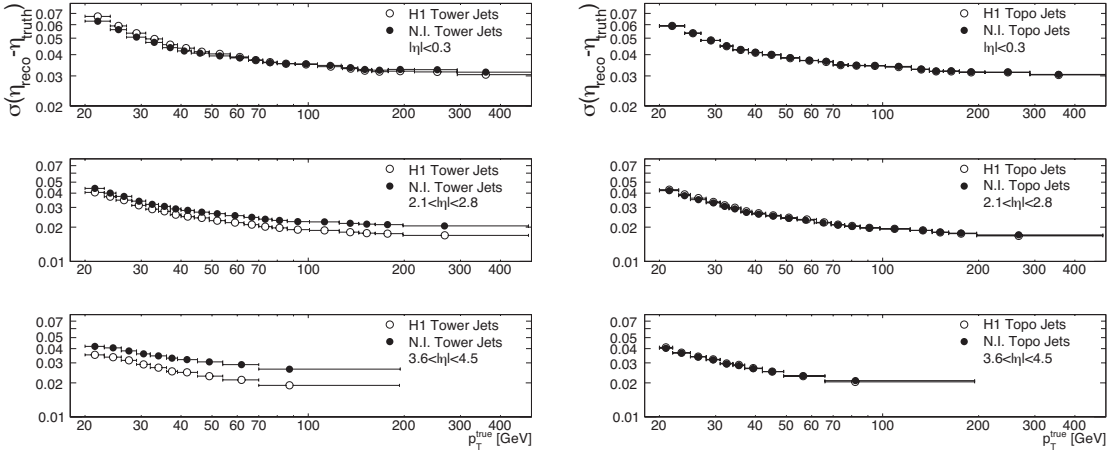

Figure 14: η resolution as a function of p_T for cone 0.4 tower (left) and topo-cluster jets (right) with the H1-style calibration (hollow points) and the numerical-inversion calibration (solid points). Three η regions are used: a central region (top, $|\eta| < 0.3$), an intermediate region (middle, $2.1 < |\eta| < 2.8$) and a forward region (bottom, $3.6 < |\eta| < 4.5$).

5 Conclusions

In this note we have motivated the need of a simple Monte Carlo-based calibration. This calibration consists of inverting the electromagnetic-scale response function as a function of p_T and η. To perform this inversion, the *numerical inversion* technique has been described and used. This technique is widely applicable for restoring a p_T-dependent response function in Monte Carlo-based (e.g.: H1-style, local-hadron) and data-driven calibrations alike.

The simple calibration provides a jet response with a mean value of 1. The jet response is constant in p_T and η within $\approx 3\%$ for the di-jet sample used in deriving the correction. A Z+jets sample with a higher content of quark jets has been used to determine the stability of this linearity studying the change

of flavor content and p_T spectrum. The linearity is maintained with a $\approx 3\%$ upward shift that can be attributed to the larger response of quark jets in the Z+jets sample.

The p_T resolution of the simple calibration has been compared to the p_T resolution of the H1-style calibration, showing a similar performance for low-p_T jets. For high-p_T jets the H1-style calibration provides a significant performance improvement over the simple calibration, especially for central jets.

The angular resolution has also been studied. Topo-cluster jets calibrated with H1-style and those calibrated with the simple calibration developed in this note are reconstructed with a similar η and ϕ resolutions. The features of the angular resolution for tower jets are currently not understood. The angular resolution studies suggest that for jets of $p_T^{\text{true}} \approx$ 20-30 GeV the matching radius between reconstructed and truth jets for performance studies should be of ≈ 0.3.

Acknowledgements

References

[1] ATLAS Collaboration, Expected Performance of the ATLAS Experiment, Detector, Trigger and Physics, CERN-OPEN-2008-020; arXiv:0901.0512.

[2] T. Barillari *et al.*, Local Hadronic Calibration, ATL-LARG-PUB-2009-001.

[3] The ATLAS Collaboration, Jet Reconstruction Performance, ATL-PHYS-PUB-2009-012.

[4] Z. Marshall, E. W. Hughes and A. Schwartzman, Track-based improvement in the jet energy resolution for ATLAS, ATL-PHYS-INT-2008-029.

[5] D. Lincoln, G. Morrow and P. Kasper, Nucl. Instrum. Meth. A **345**, 449 (1994).

Appendix A: Numerical Inversion Performance as a Baseline

In the Introduction, the need for a simple calibration was motivated partially to provide a performance baseline. This might be counter-intuitive, because a performance baseline should be given by the simplest possible set of reconstruction algorithms. A more intuitive baseline would then be the performance of the jet reconstruction at the electromagnetic scale, i.e.: before any calibration is applied. Unfortunately, the non-linearity of electromagnetic-scale jets renders their performance inappropriate for this task.

Consider Figure A-1, showing the response and fractional resolution for electromagnetic-scale and numerical-inversion jets in the barrel region. This figure shows the non-linearity of the response of
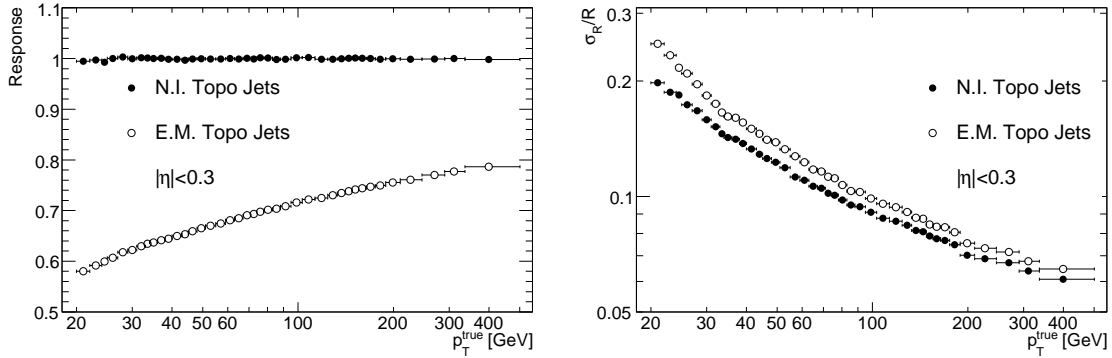

Figure A-1: Left: Response for cone 0.4 topo-cluster jets with $|\eta| < 0.3$. Right: Fractional resolution for cone 0.4 topo-cluster jets with $|\eta| < 0.3$. Jets are shown before calibration (electromagnetic-scale jets, hollow points) and after the numerical-inversion calibration (solid points).

electromagnetic-scale jets. The response for the numerical-inversion calibration is fixed at 1 for the full p_T range, and thus the curve showing p_T^{reco} vs p_T^{true} will be linear and with a slope of 1. However, it also shows that the fractional resolution is systematically better for numerical-inversion jets than for electromagnetic-scale jets. This may seem at first surprising, because all that the numerical-inversion calibration does is to invert the response. There is no aim at improving resolution, yet this figure shows that there is such an improvement.

This 'improvement' is associated with the restoration of the linearity of the response. That is, the value of the resolution will be modified in the process of restoring linearity to the response. Since we have no use for jets unless their response is linear with p_T, the fractional resolution for a jet calibration with a non-linear response is not a meaningful quantity. The process by which the fractional resolution changes is illustrated in Figure A-2. This figure shows what happens in a fixed-p_T^{true} bin when the numerical-inversion calibration is applied as a function of $p_{T,\text{EM}}^{\text{reco}}$. Jets with a low response are reconstructed with lower $p_{T,\text{EM}}^{\text{reco}}$, and therefore receive a larger correction. Similarly, jets with a high response are reconstructed with higher $p_{T,\text{EM}}^{\text{reco}}$, and therefore receive a smaller correction.

Application of the inversion results in an apparent improvement in the jet energy resolution because the response of electromagnetic-scale jets is monotonically increasing. However, for monotonically decreasing response functions, the result will be the opposite, that is, the calibration process will result in an apparent deterioration of the fractional resolution.

One example is the response of tower jets calibrated in H1 style in the forward region, as shown in Figure 6. The form of this response indicates that the actual fractional resolution will be worse than demonstrated in Figure 12, once the response of H1-style calibration jets is made linear using numerical inversion or using other techniques.

For this reason, only the fractional resolutions of calibrations with a linear response should be studied.
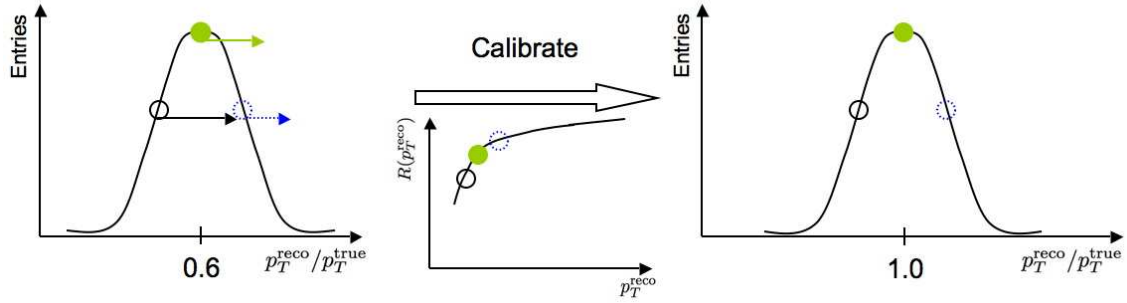
15

Figure A-2: Illustration of the process that makes the numerical inversion fractional resolution better than that of electromagnetic-scale jets. Lower-response jets receive a larger correction than higher-response jets. This causes the fractional width (width/mean) of the Gaussian response distribution to be smaller after the correction.

The numerical-inversion calibration is the simplest calibration that provides a linear response, and thus a meaningful baseline for performance studies.

Appendix B: Fiducial Cuts in the Z sample

The non-ideal conditions of the calorimeters in the Z +jets sample create 'holes' of lower jet response. In order to avoid these holes and make meaningful comparisons with the di-jet sample a set of fiducial cuts described in Section 2 is applied. These cuts were determined identifying these holes in plots showing the response as a function of ϕ in the different η regions. These plots are shown for topo-cluster jets for the affected η regions in Figure B-1. The regions left out by our fiducial cuts (listed in Table 2) are
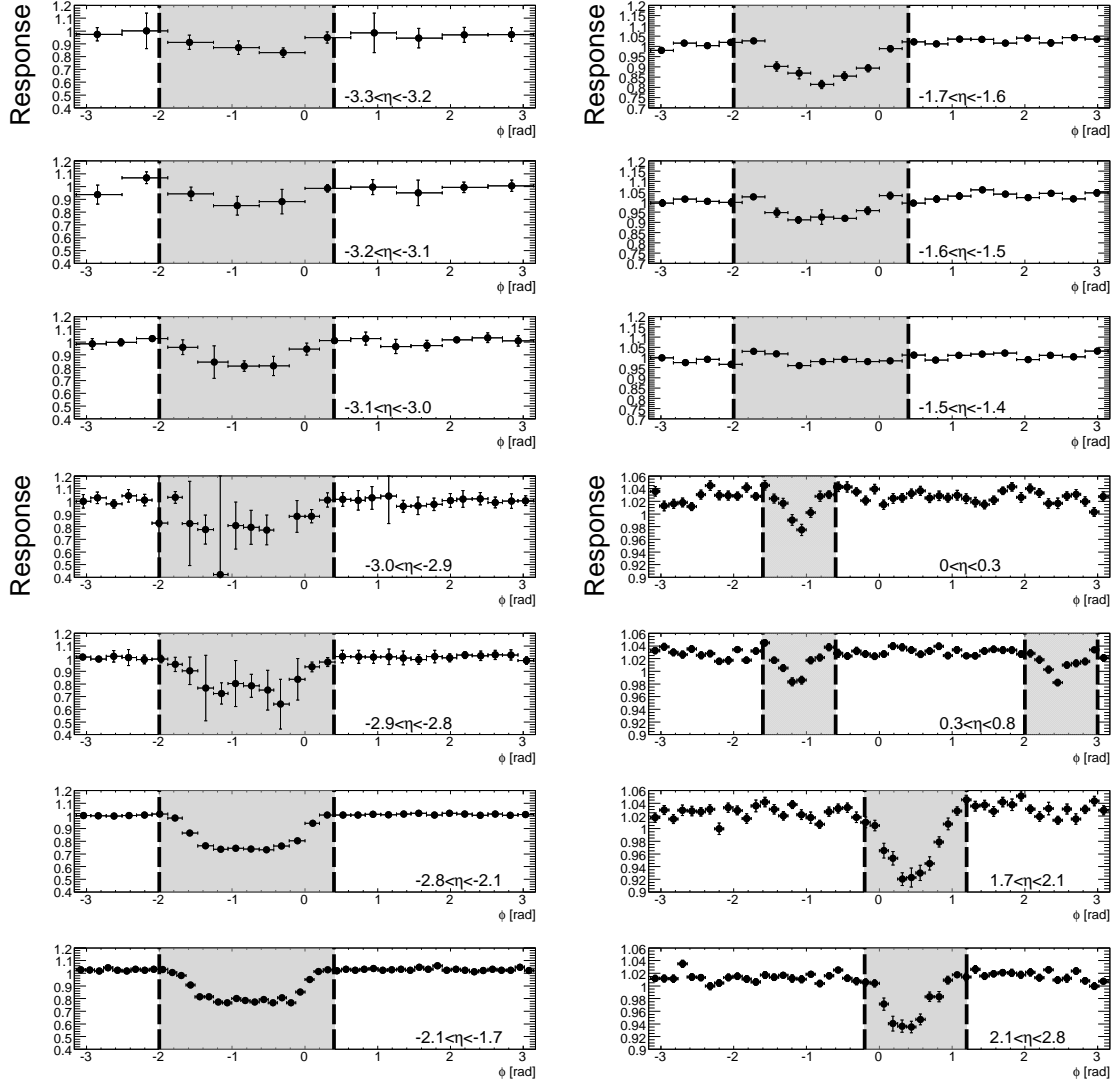

Figure B-1: Response as a function of ϕ for cone 0.4 topo-cluster jets from the di-jet samples with p_T^{true} > 20 GeV. The numerical-inversion (which is ϕ-independent) has been applied. The regions of low response correspond to areas where part of the calorimeter read-out was switched off. The η regions shown are those where fiducial cuts were applied. Jets in the shaded areas were left out of the event selection to avoid biases in these studies.

shaded.

Appendix C: Numerical Inversion Correction for The Full Detector

In this appendix we provide the calibration constants for the full η range studied and show the response and resolution plots as a function of p_T^{true} for all the η regions that were not shown in the main text of this note. The calibration function is:

$$\sum_{i=0}^{4} \frac{a_i}{(\ln(p_{T,\text{EM}}^{\text{reco}}[\text{ GeV}]))^i}, \tag{C-1}$$

with $a_0 = 1$. This function is defined for all the η regions outlined in Section 2 and it is different for tower and topo-cluster jets. The values of a_i for $i = 1, ..., 4$ in all these regions are shown in Tables C-1 and C-2.

	$|\eta|$ range	a_1	a_2	a_3	a_4
	$[0, 0.3]$	-5.721×10^{-1}	-8.542	3.370×10^1	-3.670×10^1
	$[0.3, 0.8]$	-4.384×10^{-1}	-9.780	3.736×10^1	-4.085×10^1
	$[0.8, 1.4]$	-5.979×10^{-1}	-8.582	3.087×10^1	-3.099×10^1
	$[1.4, 1.5]$	-1.506	-2.568	1.676×10^1	-1.893×10^1
	$[1.5, 1.6]$	-2.552×10^{-1}	-1.051×10^1	3.546×10^1	-3.478×10^1
	$[1.6, 1.7]$	-1.228×10^{-2}	-1.177×10^1	3.840×10^1	-3.746×10^1
Cone 0.4 tower jets	$[1.7, 2.1]$	4.233×10^{-1}	-1.423×10^1	4.598×10^1	-4.672×10^1
	$[2.1, 2.8]$	-3.102×10^{-1}	-6.946	2.496×10^1	-2.685×10^1
	$[2.8, 2.9]$	-1.135×10^{-1}	-9.701	3.456×10^1	-3.647×10^1
	$[2.9, 3.0]$	-2.035	7.907	-2.147×10^1	2.300×10^1
	$[3.0, 3.1]$	-2.153	7.564	-1.905×10^1	1.966×10^1
	$[3.1, 3.2]$	-2.593	7.677	-1.538×10^1	1.461×10^1
	$[3.2, 3.3]$	-3.556	1.098×10^1	-1.630×10^1	1.058×10^1
	$[3.3, 3.4]$	4.735×10^{-1}	-2.592×10^1	9.663×10^1	-1.042×10^2
	$[3.4, 3.5]$	1.645	-2.605×10^1	7.775×10^1	-7.205×10^1
	$[3.5, 3.6]$	2.197	-2.868×10^1	8.727×10^1	-8.692×10^1
	$[3.6, 4.5]$	-3.504	2.616×10^1	-9.008×10^1	1.061×10^2

Table C-1: Calibration constants for cone 0.4 tower jets.

Figures C-1 (tower jets) and C-2 (topo-cluster jets) show the response as a function of p_T^{true} for jets from the di-jet sample in all η regions, not previously given in Section 4.1. Similarly, the fractional jet energy resolution as a function of p_T^{true} for jets from the di-jet sample in all η regions is shown in Figures C-3 (tower jets) and C-4 (topo-cluster jets). The features of these response and fractional jet energy resolution functions are similar to those already discussed, so these plots are only provided for reference.

	$|\eta|$ range	a_1	a_2	a_3	a_4
	$[0,0.3]$	-6.182×10^{-1}	-7.144	2.589×10^1	-2.679×10^1
	$[0.3,0.8]$	-5.789×10^{-1}	-7.280	2.544×10^1	-2.571×10^1
	$[0.8,1.4]$	-4.978×10^{-1}	-8.745	2.908×10^1	-2.809×10^1
	$[1.4,1.5]$	-1.460	-2.214	1.352×10^1	-1.532×10^1
	$[1.5,1.6]$	-5.717×10^{-1}	-6.217	1.791×10^1	-1.429×10^1
	$[1.6,1.7]$	-1.010×10^{-1}	-9.921	2.927×10^1	-2.629×10^1
Cone 0.4 topo jets	$[1.7,2.1]$	2.432×10^{-1}	-1.198×10^1	3.606×10^1	-3.465×10^1
	$[2.1,2.8]$	-8.869×10^{-2}	-8.888	3.086×10^1	-3.277×10^1
	$[2.8,2.9]$	3.713×10^{-1}	-1.359×10^1	4.766×10^1	-5.151×10^1
	$[2.9,3.0]$	3.874×10^{-1}	-1.553×10^1	5.691×10^1	-6.362×10^1
	$[3.0,3.1]$	-1.061	-2.373	1.360×10^1	-1.594×10^1
	$[3.1,3.2]$	7.309×10^{-1}	-2.394×10^1	8.623×10^1	-9.183×10^1
	$[3.2,3.3]$	-7.805×10^{-1}	-1.622×10^1	7.336×10^1	-8.509×10^1
	$[3.3,3.4]$	-3.461	1.225×10^1	-2.298×10^1	1.985×10^1
	$[3.4,3.5]$	1.208	-2.204×10^1	6.836×10^1	-6.625×10^1
	$[3.5,3.6]$	1.863×10^{-1}	-7.876	1.979×10^1	-1.608×10^1
	$[3.6,4.5]$	6.530×10^{-1}	-1.529×10^1	5.178×10^1	-5.553×10^1

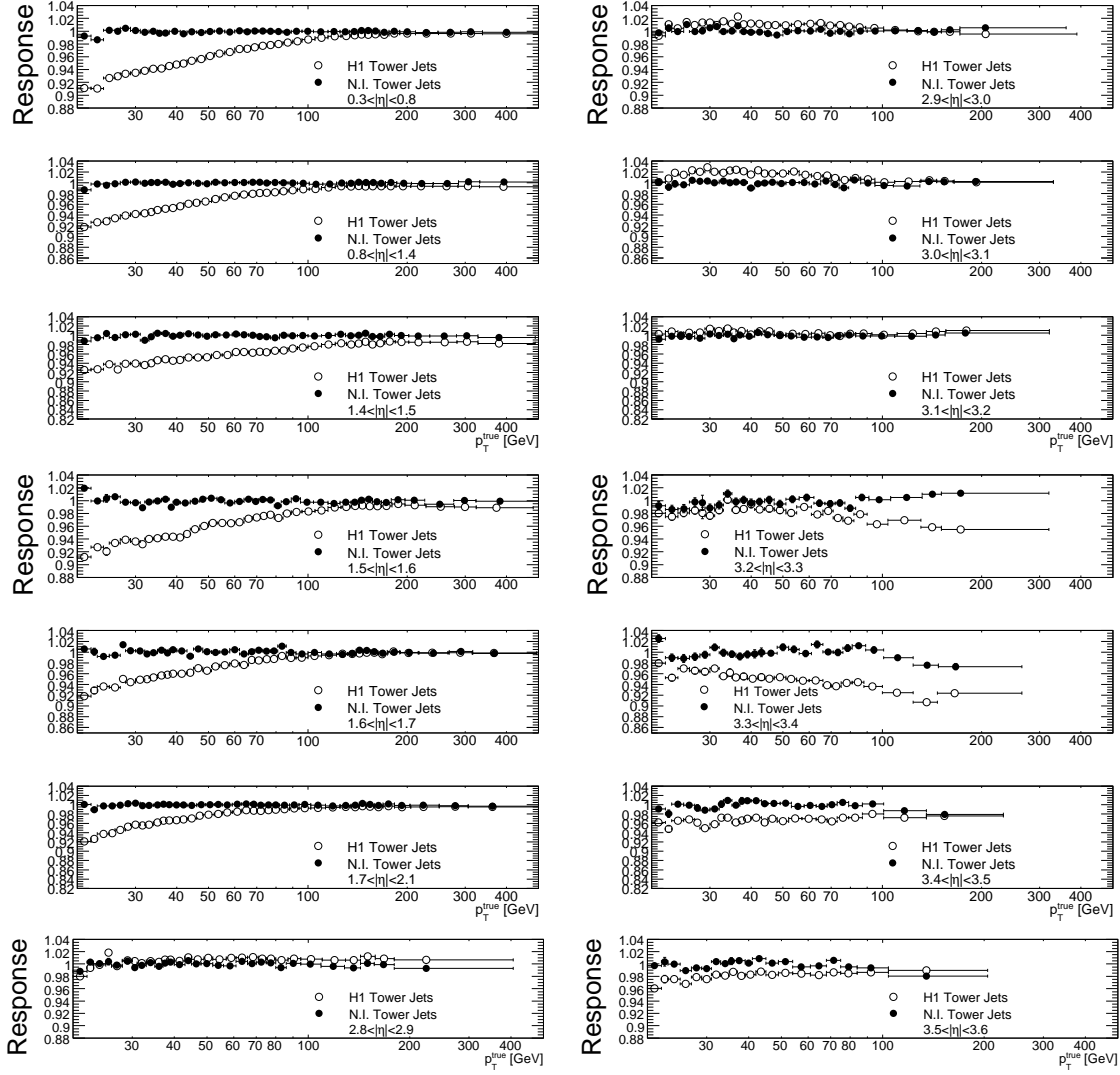Table C-2: Calibration constants for cone 0.4 topo-cluster jets.

Figure C-1: Jet response as a function of p_T^{true} for cone 0.4 tower jets in different η regions where the numerical-inversion calibration was calculated. Jets calibrated with the H1-style calibration (hollow points) and with the numerical-inversion calibration (solid points) are shown.
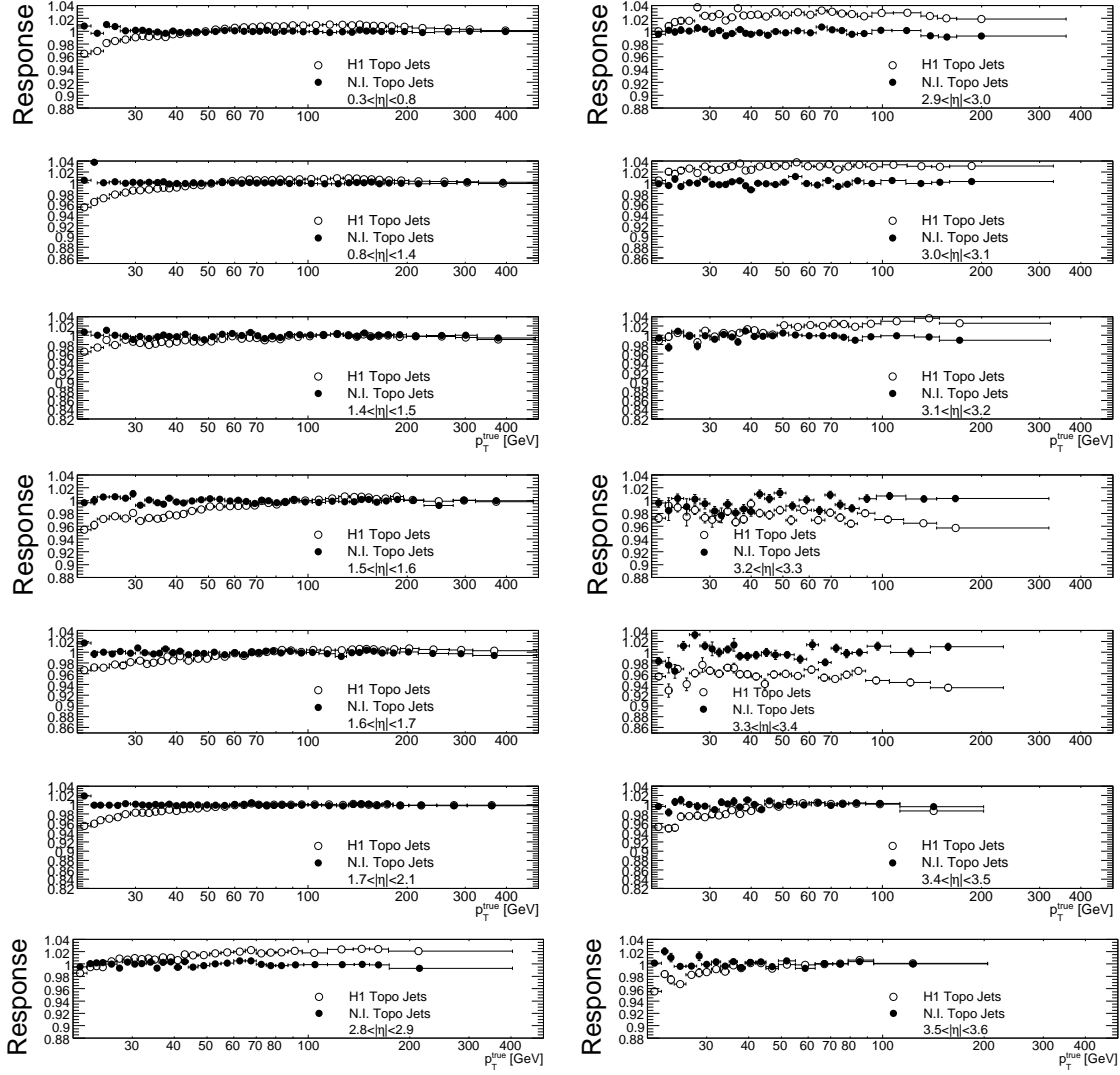
Figure C-2: Jet response as a function of p_T^{true} for cone 0.4 topo-cluster jets in different η regions where the numerical-inversion calibration was calculated. Jets calibrated with the H1-style calibration (hollow points) and with the numerical-inversion calibration (solid points) are shown.
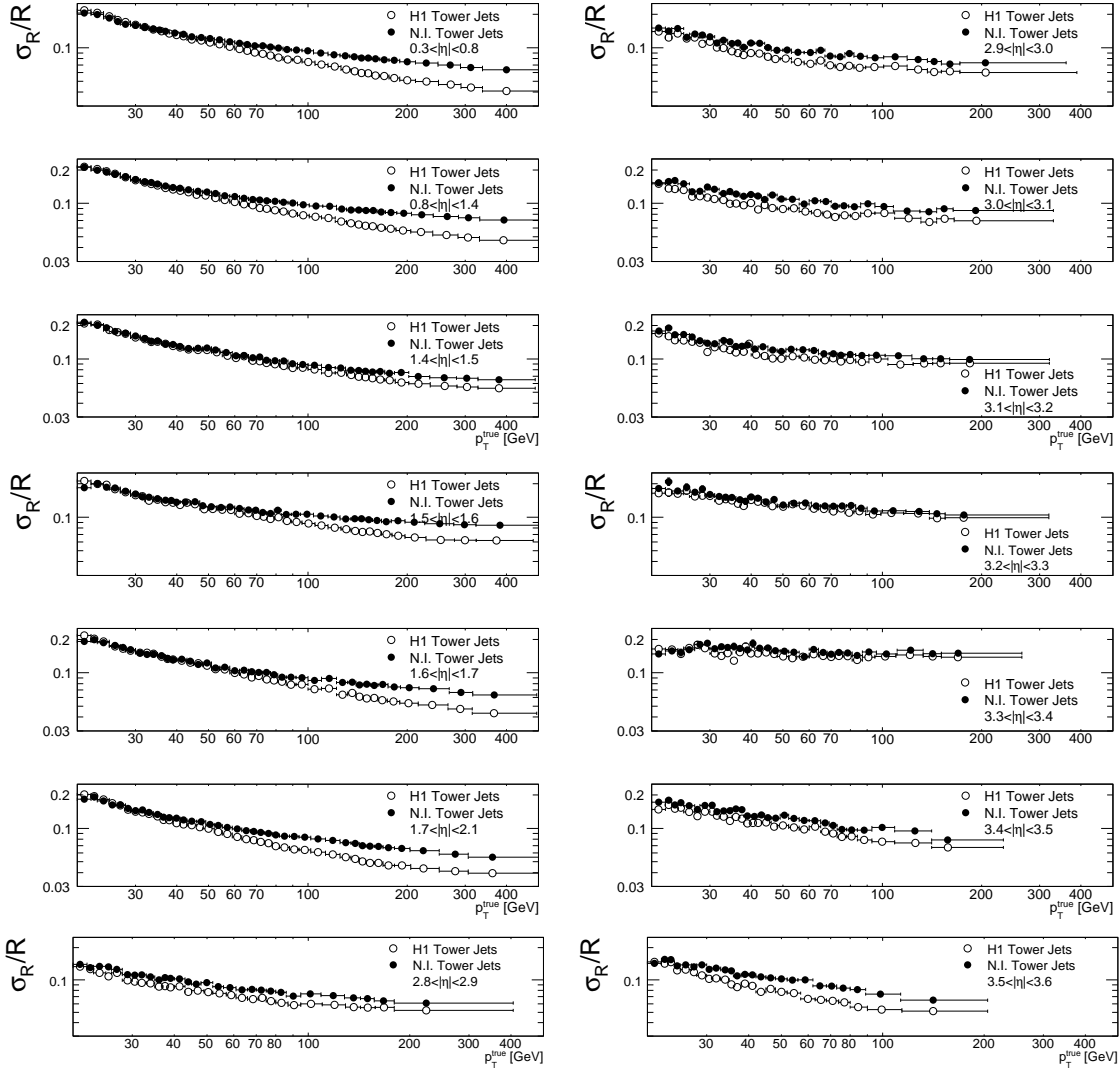
Figure C-3: Jet fractional resolution as a function of p_T^{true} for cone 0.4 tower jets in different η regions where the numerical-inversion calibration was calculated. Jets calibrated with the H1-style calibration (hollow points) and with the numerical-inversion calibration (solid points) are shown.
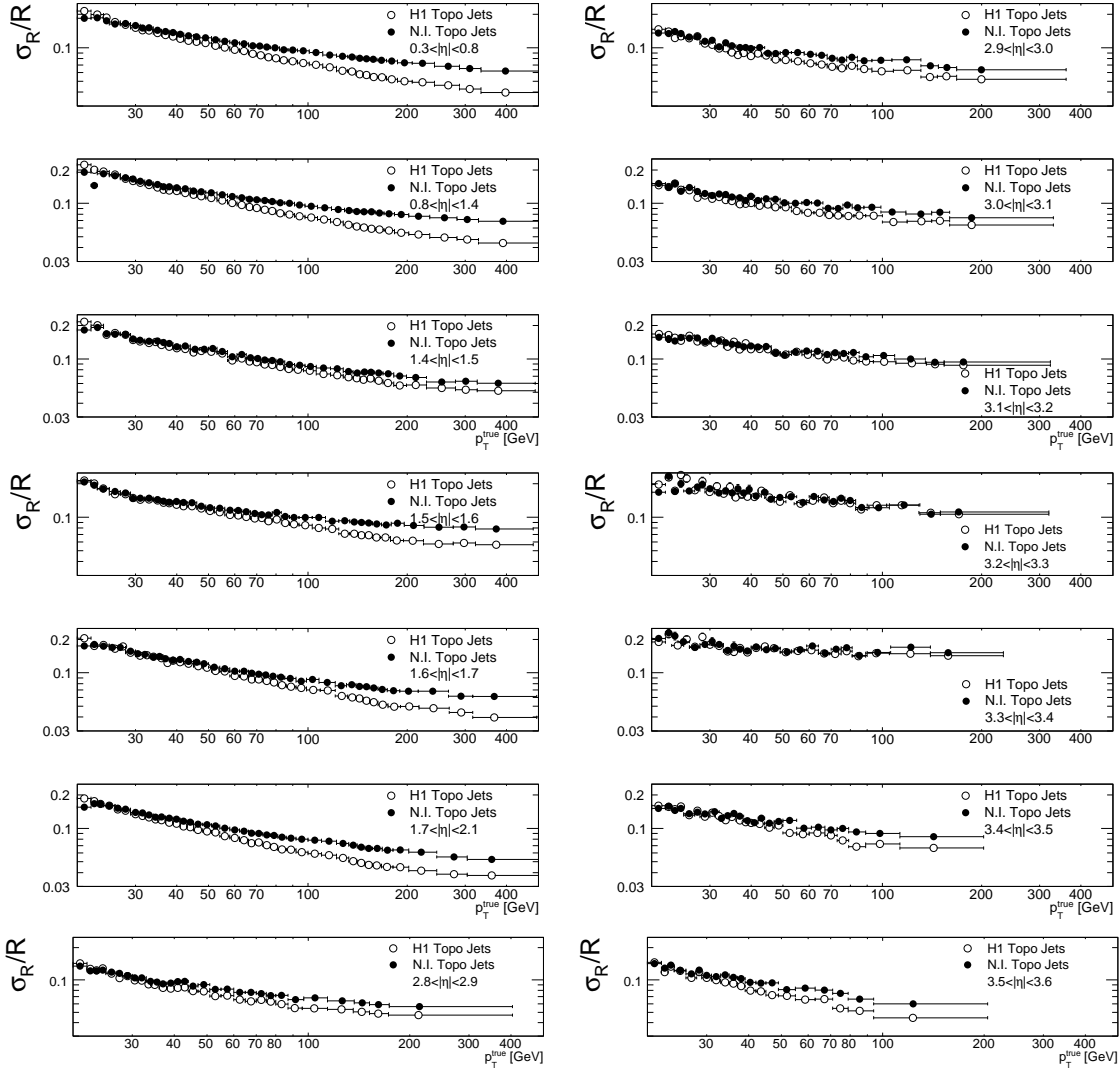
Figure C-4: Jet fractional resolution as a function of p_T^{true} for cone 0.4 topo-cluster jets in different η regions where the numerical-inversion calibration was calculated. Jets calibrated with the H1-style calibration (hollow points) and with the numerical-inversion calibration (solid points) are shown.